Spatiotemporal Registration of 3-D Multi-perspective Ultrasound Images of Abdominal Aortic Aneurysms

Ultrasound in Med. & Biol., Vol. 49, No. 1, pp. 318–332, 2023

0301-5629/$ - see front matter

https://doi.org/10.1016/j.ultrasmedbio.2022.09.005

● *Original Contribution*

SPATIOTEMPORAL REGISTRATION OF 3-D MULTI-PERSPECTIVE ULTRASOUND IMAGES OF ABDOMINAL AORTIC ANEURYSMS

Marloes Sjoerdsma,[*,†] Sabine C.F.P.M. Verstraeten,[*,‡] Esther J. Maas,[*,†]
Frans N. van de Vosse,[‡] Marc R.H.M. van Sambeek,[†] and Richard G.P. Lopata[*]

[*] Photoacoustics & Ultrasound Laboratory Eindhoven (PULS/e), Department of Biomedical Engineering, Eindhoven University of Technology, Eindhoven, The Netherlands; [†] Department of Vascular Surgery, Catharina Hospital Eindhoven, Eindhoven, The Netherlands; and [‡] Cardiovascular Biomechanics Group, Department of Biomedical Engineering, Eindhoven University of Technology, Eindhoven, The Netherlands

(*Received* 4 *April* 2022; *revised* 2 *August* 2022; *in final form* 7 *September* 2022)

Abstract—Methods for patient-specific abdominal aortic aneurysm (AAA) progression monitoring and rupture risk assessment are widely investigated. Three-dimensional ultrasound can visualize the AAA's complex geometry and displacement fields. However, ultrasound has a limited field of view and low frame rate (*i.e.,* 3–8 Hz). This article describes an approach to enhance the temporal resolution and the field of view. First, the frame rate was increased for each data set by sequencing multiple blood pulse cycles into one cycle. The sequencing method uses the original frame rate and the estimated pulse wave rate obtained from AAA distension curves. Second, the temporal registration was applied to multi-perspective acquisitions of the same AAA. Third, the field of view was increased through spatial registration and fusion using an image feature–based phase-only correlation method and a wavelet transform, respectively. Temporal sequencing was fully correct in aortic phantoms and was successful in 51 of 62 AAA patients, yielding a factor 5 frame rate increase. Spatial registration of proximal and distal ultrasound acquisitions was successful in 32 of 37 different AAA patients, based on the comparison between the fused ultrasound and computed tomography segmentation (95th percentile Haussdorf distances and similarity indices of 4.2 ± 1.7 mm and 0.92 ± 0.02 mm, respectively). Furthermore, the field of view was enlarged by 9%–49%. (E-mail: m.sjoerdsma@tue.nl)

Key Words: **Image registration, 3-D ultrasound, Multi-perspective ultrasound, Field of view, Frame rate, Abdominal aortic aneurysm.**

INTRODUCTION

An abdominal aortic aneurysm (AAA) is a progressive local widening in the abdominal aorta. AAAs are usually asymptomatic until rupture, which can lead to large, life-threatening hemorrhages with a mortality of approximately 80% (Reimerink et al. 2013). Surgical treatment is advised only in case rupture risk outweighs the risk of the intervention. Current clinical guidelines generally advise intervention for AAAs with a maximal diameter exceeding 55 or 50 mm in men or women, respectively, or when its growth rate surpasses 10 mm/y (Anders et al. 2018; Chaikof et al. 2018). However, many larger AAAs remain stable, whereas 2%–10% of all AAAs rupture before the current clinical threshold diameter or growth rate is reached (Reed et al. 1997; Lederle et al. 2002).

Previous studies proposed more patient-specific methods to assess AAA rupture risk using aortic volume measurements (Kauffmann et al. 2012), (peak) wall stress analysis (Fillinger et al. 2003) and aortic stiffness quantification (Wilson et al. 2003). Different imaging modalities have been used for patient-specific rupture risk evaluation, such as computed tomography (CT), magnetic resonance imaging and ultrasound (US) (Raghavan and Vorp 2000; Fillinger et al. 2003; Merkx et al. 2009; Erhart et al. 2015; Gasser 2016; Indrakusuma et al. 2016; Van Disseldorp et al. 2019). Contrarily to other imaging modalities, US can be used to monitor the individual AAAs over longer periods, as US is non-invasive, safe, inexpensive and easily accessible.

Address correspondence to: Marloes Sjoerdsma, P.O. Box 513, 5600 MB Eindhoven, The Netherlands. E-mail: m.sjoerdsma@tue.nl

Furthermore, in addition to aortic wall stress and stiffness, investigation of the wall displacement and strain is possible with US (Han and Fung 1995; Karatolios et al. 2013; Van Disseldorp et al. 2019). For computation of the patient-specific material properties, an accurate AAA geometry and displacement field are required.

Although time-resolved 3-D (3-D+t) ultrasound is a suitable imaging modality to capture complex organ shapes and contraction patterns, AAA imaging is limited by a restricted field-of-view (FOV) and a relatively low frame rate (van Disseldorp et al. 2016a).

Forty to forty-five percent of the AAAs require multiple acquisition in the proximal−distal direction (*i.e.,* multi-perspective ultrasound) to capture the entire geometry of the aneurysm. Segmentation-based registration algorithms for these multi-perspective images have been proposed (Van Disseldorp et al. 2020b). These segmentation-based registration methods strongly rely on the segmentation performance and thus require a relatively high AAA lumen−wall contrast. For registration of US acquisitions of the aorta, image features visible in both acquisitions are required, because for tubelike structures, computation of the rotation and translation around and along the longitudinal axis is challenging. Alternatively, extended-FOV imaging has also been employed to obtain US acquisitions with a large FOV. In this method, real-time images are stitched to obtain a large, although static, B-mode image (Barberie et al. 1998; Baba et al. 2000; Elliott 2006; Yerli and Eksioglu 2009). In addition, free-hand (probe-tracked) ultrasound has been used to obtain static, large FOV B-mode images (Xiao et al. 2002; Rana and Wakeling 2011; Van den Heuvel et al. 2019; Zielinski et al. 2019; De Ruijter et al. 2020).

Furthermore, 3-D+t AAA imaging typically presents frame rates lower than 10 Hz. Most previous studies computed the 3-D+t AAA wall displacements and volume changes directly from end-diastole to end-systole (Van Disseldorp et al. 2019), created a sparse 3-D motion field using 2-D biplane US imaging (Petterson et al. 2021) or stitched multiple smaller volume sections together (Wittek et al. 2013). Three-dimensional AAA elastic behavior assessment is expected to benefit greatly from a higher temporal resolution, which could be achieved by combining and sequencing multiple blood pulse wave cycles of the AAA US images into one artificial pulse wave cycle with an increased frame rate. Plane wave imaging has also had promising results (Yang et al. 2014; De Hoop et al. 2020), though this technique is still clinically unavailable. Additionally, deep learning has been used in previous studies to successfully increase the frame rate (Niklaus et al. 2017; Senouf et al. 2018). Unfortunately, a ground truth data set required for training the deep learning model is not available for this application.

The objective of this study was to create a method to increase both the field of view and temporal resolution of AAA US acquisitions. The workflow proposed includes multi-perspective ultrasound acquisitions and temporal sequencing, temporal and spatial registration and fusion algorithms. The full spatiotemporal registration workflow is created to combine multiple acquisitions of the aorta using different probe positions to yield both an increased temporal resolution and increased field of view. Yet, the temporal sequencing section can also be applied to individual 3-D+t aortic acquisitions to increase the frame rate.

METHODS

Spatiotemporal registration workflow

The workflow proposed is created for US imaging of AAAs that require multiple acquisitions to capture their entire geometry. For these AAAs, proximal and distal 3-D+t US acquisitions were obtained consecutively on a sagittal plane along the long axis of the AAA using a clinical US scanner. The proximal and distal AAA US images were registered in time and space using the spatiotemporal registration algorithm, which consists of three different components. First, the proximal and distal 3-D+t AAA acquisitions are temporally sequenced by combining and sorting multiple blood pulse wave cycles into one blood pulse wave cycle with a higher frame rate density. Second, the corresponding temporally sequenced acquisitions are registered in time. Third, after temporal registration, the time-matched AAA volumes are spatially registered and fused to create the final AAA US acquisition with an increased frame rate and field of view.

Workflow part 1: Temporal sequencing

Temporal sequencing was applied to increase the frame rate. For temporal sequencing and registration, the pulse phase (*i.e.,* relative position within the blood pulse cycle) of all frames had to be computed. Once the pulse phases of all frames were determined, the frames could be ordered to create a 3-D+t data set with improved frame rate. The workflow proposed for temporal sequencing (and, thus, pulse phase computation) is illustrated in Figure 1 and described in the following.

First, the original 3-D+t AAA ultrasound image is filtered using an Euclidean shortening flow (ESF) filter using a standard deviation of 0.8 voxels, step size of 0.4 voxels and 12 steps (Alvarez et al. 1993). The ESF filter blurs predominantly along rather than across edges, which preserves the image features. This filter was used for elimination of acoustic shadows, reverberation artifacts and US speckle (Fig. 1, step 1).

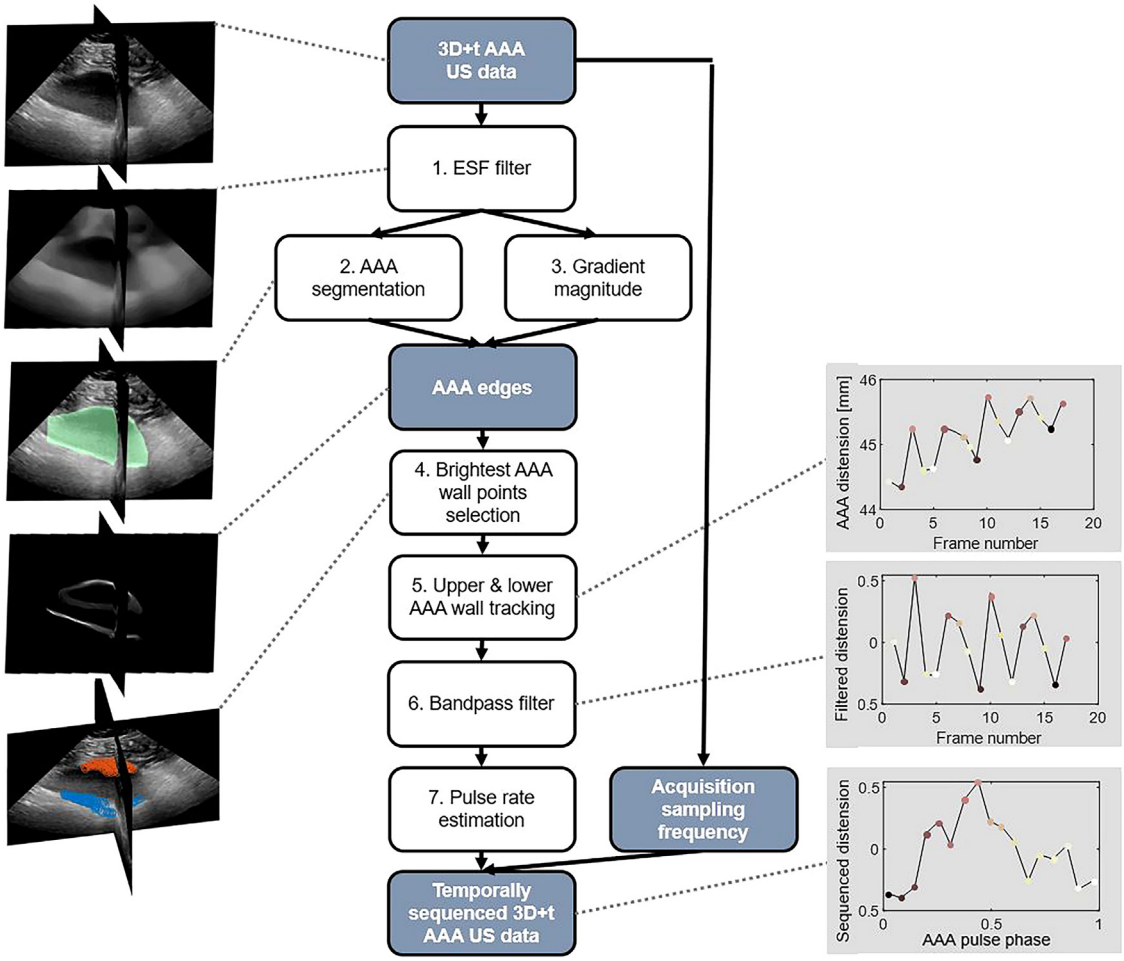

Fig. 1. Temporal sequencing of the abdominal aortic aneurysm (AAA) ultrasound (US) acquisitions. (1) The original US data were filtered using an Euclidean shortening flow (ESF) filter. (2) The inner wall of the first frame of the ESF-filtered data was segmented using a Star−Kalman method. (3) The gradient magnitude of the filtered data is computed using the Sobel gradient operator. Next, the dilated segmentation was applied as a mask to the first gradient magnitude image to obtain the gradient magnitude edges of the AAA. (4) The brightest points on the anterior and posterior walls were selected, shown in *red and blue*, respectively. (5) These selected wall points were tracked in the z-direction (*i.e.,* depth or vertical direction) over time, resulting in AAA distension curves. (6) These distension curves were bandpass filtered. (7) The Lomb−Scargle power spectral density was created from the bandpass-filtered signal. The highest peak within the spectral density function is the estimated pulse wave rate. Finally, the US acquisition could be temporally sequenced using the estimated pulse wave rate and US frame rate. The subimages in this figure are all derived from an AAA patient's data set.

Second, the inner wall of the first frame of the 3-D+t AAA acquisition was segmented (Fig. 1, step 2). During the segmentation, first, an ellipse was fitted in the middle volume slice (transverse view). Subsequently, the AAA was detected in the consecutive slices using the Star−Kalman method, propagating outward until the middle 60% of the ultrasound volume was segmented (De Ruijter et al. 2020). The radius of the AAA segmentation was then dilated by 2 mm to envelop the outer AAA walls. Next, the gradient magnitudes of the ESF-filtered image were computed using the Sobel gradient operator (Fig. 1, step 3). Subsequently, the dilated AAA segmentation was used as a mask and applied to the gradient magnitude image of the first frame, resulting in the AAA wall edges. The five thousand brightest points of the anterior and posterior AAA wall were selected from the masked gradient magnitude image. For computation efficiency, selected voxels positioned within a 4-voxel radius from another selected point were excluded. Outliers were removed by dividing the points on the anterior and posterior wall into clusters with a minimal distance of 50 voxels using a *k*-means clustering method. In case a cluster is situated farther

than 1 cm from the most anterior and posterior cluster, this cluster was discarded (Fig. 1, step 4).

The selected points on the anterior and posterior walls in the gradient magnitude images were tracked over time, providing an estimate of the AAA's distension curve (Fig. 1, step 5). For AAA distension curve computation, regions with high lumen−wall contrast were selected and tracked in the US z-direction (similar to the anterior−posterior direction) over time. Points in high lumen−wall contrast regions were selected, as tracking of these regions is most accurate and robust.

For each selected point on the anterior and posterior wall, the best matching 5- × 5- × 5-voxel cubic candidate region is selected on the next frame within a search region of $n \times 5 \times 5$ ($z \times x \times y$) voxels, with n being equal to 10% of the AAA's distension curve's maximum. The best candidate is selected by shifting the previous frame's candidate region over the search region of the current frame using the energy function

$$E = \frac{\sum_i w(i)\left|g(c_i) - g(c_{i+1})\right|}{2\sum_i w(i)} \quad (1)$$

where g is the gradient magnitude value of the cubic region (5 × 5 × 5 voxels) surrounding the selected point on frame i (c_i) and a possible corresponding candidate cubic region on frame $i+1$ (c_{i+1}), and $w(i)$ is a convex weight function that is maximal at the center of the cubic region. For each selected point on frame i, the candidate point on frame $i+1$ with the lowest energy (E) was selected.

The AAA's distension curve was estimated by obtaining the mean distance between the tracked anterior and posterior points per frame. AAA distension curves were filtered to correct for AAA motion unrelated to the contraction of the vessel itself (*e.g.,* probe motion, respiration-related motion) (Fig. 1, step 6). For the filtering of distension curves, first, absolute AAA distension curve values higher than $\mu + 2 * \sigma$ were discarded, with μ the mean and σ the standard deviation of the distension curve. Next, a bandpass filter was applied to the AAA distension curves with cutoff values of 40 and 100 cycles/min and a steepness of 15% of the passband frequency. From the bandpass-filtered distension curves, the pulse wave rate was estimated using the Lomb−Scargle power spectral density estimate, which is a least-squares spectral analysis method (Lomb 1976) (Fig. 1, step 7). The peaks within the spectral density graph represent the most likely pulse wave rate values. In case multiple peaks are observed, the best match in pulse wave rates between the proximal and distal acquisitions was chosen. This best match was computed by summing the heights of the spectral density peaks, followed by multiplication with the difference in pulse wave rates between the proximal and distal acquisitions. From these weighted differences, the absolute minimum was determined, which corresponds to the most likely pulse wave rates for the proximal and distal acquisitions.

Finally, the 3-D+t AAA acquisition could be temporally sequenced, meaning the multiple pulse wave cycles obtained in the acquisition can be merged into one pulse wave cycle with a higher frame density using the estimated pulse wave rate and the frame rate. The pulse phases p_i of the frame numbers (i) within an acquisition were computed using

$$p_i = \mathrm{mod}(i \cdot f_{HR}/f_s, 1) \quad (2)$$

where mod is the modulus, f_s the frame rate in hertz and f_{HR} the pulse wave rate in hertz. The pulse wave rate is assumed to be constant, as the acquisitions were obtained with steady-state blood pulse wave rate and during breath hold.

Workflow part 2: Temporal registration

Temporal registration of the sequenced proximal and distal acquisitions was achieved by first aligning the end-systolic points within the pulse wave cycle, followed by pairing of the other frames. First, the end-systolic frame numbers of the sequenced AAA proximal and distal distension curves were estimated by fitting a second-order Fourier curve of a single period through the distension curves (Fig. 2, step 1). Subsequently, the determined end-systolic frames of the sequenced proximal and distal acquisitions were aligned in the pulse phase (Fig. 2, *red dotted line*). Second, once the end-systolic frames were aligned, the other frames of the proximal and distal acquisitions were paired. The pairing was accomplished by coupling frames with the minimum difference in pulse phase (Fig. 2, step 2). Unpaired frames were discarded.

Workflow part 3: Spatial registration and image fusion

The temporally registered proximal and distal AAA acquisitions had to be registered spatially prior to fusing the acquisitions into one data set with an enlarged field-of-view. The full spatial registration and fusion algorithm overview is displayed in Figure 3. First, the ultrasound images were converted into isometric data by upsampling all voxel dimensions to the smallest voxel dimension length of corresponding proximal and distal acquisitions. In addition, the volume sizes of the proximal and distal acquisitions were made equal in size using zero padding (Fig. 3, step 1).

Second, the initial spatial registration is computed for every proximal−distal frame set separately (Fig. 3, step 2). The initial registration was computed iteratively

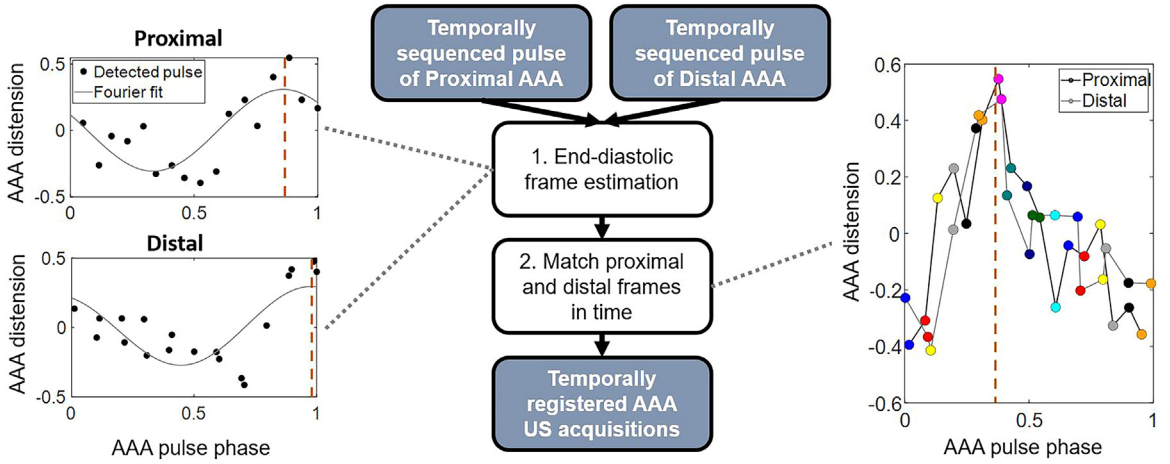

Fig. 2. Temporal registration of temporally sequenced proximal and distal US acquisitions. (1) The end-systolic frames (*red dotted line*) are determined using a second-order Fourier fit (*gray curve*) through the temporally sequenced abdominal aortic aneurysm (AAA) distension curves (*black dots*). (2) After alignment of the end-systolic frames (*red dotted line*), the other frames are paired with a minimal difference in pulse phase (identical colors of the red spectrum indicate matched frames of the proximal [*black line*] and distal [*gray line*] US acquisitions).

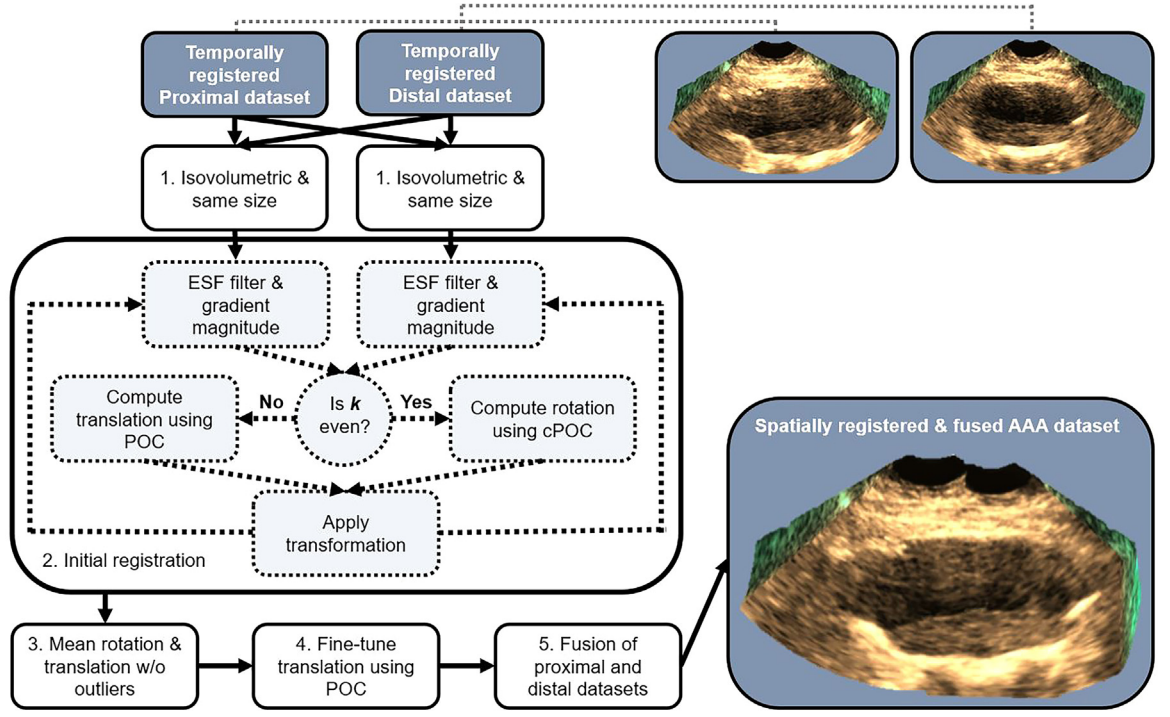

Fig. 3. Spatial registration and fusion workflow of the previously temporally registered proximal and distal acquisitions. (1) The acquisitions are converted to isovolumetric data sets with isometric voxels sizes and identical volume sizes. (2) The initial registration of all proximal−distal frame sets is performed iteratively, using seven iteration steps (k). In case k is uneven, the translation between the binarized, proximal and distal, gradient magnitude images is computed using phase-only correlation (POC). In case k is even, the rotation is computed over one of the defined axes of rotation using cylindrical phase-only correlation (cPOC). At the end of each iteration step, the transformation is applied to the isovolumetric image, after which the next iteration step is started. (3) The average rotation and translation are calculated excluding the 20% most extreme values. The averaged rotation and translation are applied to the original isometric acquisition. (4) The translations are tweaked for every proximal−distal frame set using POC to counteract probe motion that occurred during the acquisitions. (5) The spatially registered acquisitions are fused using 3-D wavelets. ESF = Euclidean shortening flow.

using seven steps. In the even iterations, the translation between the proximal and distal frames was computed, whereas the rotation over one of the three Euler rotation axes was calculated in the odd iterations. The Euler axes of rotation were defined as rotation around, and in the order of, the US y-, z- and x-axes (corresponds to approximately the elevational, axial and lateral axes, respectively). Every iteration started with the application of the ESF filter to the isometric proximal and distal acquisitions, as described under Workflow Part 1: Temporal Sequencing. Subsequently, the AAA walls were selected through gradient magnitude computation and binarization in which the 0.1% highest-intensity voxels were set to 1. Then, either the translation or rotation was computed depending on the iteration step number. The translations were estimated using phase-only correlation (POC), as a difference in phase in the Fourier spectrum corresponds to a translational shift in the spatial domain (Zhang et al. 2013). The phase-only correlation spectrum was computed using

$$S_{\mathrm{POC}}(x,y,z) = F^{-1}\left[e^{i2\pi\left(\frac{u\Delta x}{N_1}+\frac{v\Delta y}{N_2}+\frac{w\Delta z}{N_3}\right)}\right] \quad (3)$$

where F^{-1} is the inverse discrete Fourier transform, (u,v,w) are the discrete spatial frequencies in the Fourier domain, (x,y,z) are the coordinates in the spatial domain and $N_1 \times N_2 \times N_3$ is the volume sizes of the isometric proximal and distal acquisitions. In images obtained with other imaging modalities, the POC spectrum would have a narrow peak whose location corresponds to the translation between the two data sets. However, in ultrasound, a broader correlation spectrum is observed, induced by the difference in US wave refraction and reflection patterns between different images. The correlation spectrum was smoothed using a Gaussian filter with a standard deviation of 5 voxels. Finally, the translational shift between the proximal and distal images was found by highest peak detection within the smoothed POC spectrum. The shift range in the z-direction was limited to 0.025 m up and down, to prevent, for example, registration of the lower AAA wall in the proximal image to the top wall in the distal image.

The rotations were computed in a similar fashion; only now, the Fourier transforms of the gradient magnitude images were converted into cylindrical coordinates. A shift in the cylindrical frequency domain corresponds to a rotation over one of the Euler axes of rotation in the spatial domain. For the rotation computation, a 1-D Fourier transform sufficed, as only the estimation of the angular shift was desired. The Fourier transformed images were high-pass filtered with a cutoff value of 0.05 m, prior to the cylindrical phase-only correlation (cPOC) calculation. Equation (3) was used for the cPOC computation, although (x,y,z) was replaced with (ρ,ϕ,z), the radius, azimuth and height, respectively. The cPOC spectrum obtained was summed over the ρ and z, leading to the cPOC as a function of the angular shift ($\Delta\phi$). The resulting 1-D cPOC was smoothed using a Gaussian filter with its standard deviation being 1. The angular shift was estimated from the smoothed cPOC by detecting its highest peak. After every iteration, the computed translation or rotation was applied to the isovolumetric images prior to moving on to the next iteration. The initial registration is completed when the translation and rotations over all three rotation axes have been determined for all proximal and distal frames.

Once the initial registration has been estimated for all frames, the translations and rotations were averaged while excluding the 20% most extreme values (Fig. 3, step 3). The resulting averaged rotation will be used as the final rotation value between the proximal and distal acquisitions, whereas the translation will be fine-tuned for each separate proximal−distal frame set. Fine-tuning the translations will correct for probe motion and AAA motion unrelated to cardiac contraction and blood flow that occurred during data acquisitions. For the fine-tuning of the translations, first, the gradient magnitudes of the ESF-filtered, isometric images were computed. Then, the average rotation and translation that resulted from the initial registration were applied to all proximal and distal frame sets. Subsequently, the translation was computed for every proximal and distal frame set individually using the POC (Fig. 3, step 4).

Finally, the spatially registered proximal and distal acquisitions were fused into one data set, with an enlarged FOV capturing the complete AAA geometry (Fig. 3, step 5). During fusion, the fast 3-D complex-wavelet transform was used to preserve anatomical structures, while reducing noise. All paired frames of the proximal and distal acquisitions were fused. The frames were divided into five 3-D detail images (*i.e.,* frequency subbands) and an approximation image (Simoncelli and Freeman 1995). The 3-D detail images containing the highest-frequency subbands contained primarily noise and US speckle, whereas the lower-frequency subbands contained the anatomical structures. During fusion, the overlapping parts of the proximal and distal US pyramid-shaped fields of view were merged, after which the non-overlapping parts were stitched to the already merged section. The overlapping regions of the detail images were fused by taking the average of the highest frequency sub-band to reduce noise and the maximum of the lower frequency subbands to preserve anatomical structure. The inverse, fast, 3-D complex-wavelet transformation was applied to convert the fused

volumes back to the spatial domain, resulting in the fused multi-perspective image. Lastly, stitching artifacts were removed by assigning sinus-valued weights to the borders between the overlapping and non-overlapping sections of the proximal and distal ultrasound volumes.

Workflow performance assessment

Two different types of phantoms were used for performance evaluation of the temporal sequencing method proposed. A 3-D-printed, AAA-shaped phantom and a porcine abdominal aorta were used. The 3-D-printed AAA phantom consisted of elastic 50A resin that was heated for 10 min at 60˚C (Formlabs Form3 printer, 3D Medical Lab, Utrecht, Netherlands). The porcine aorta was a slaughterhouse waste product. The porcine AA US data used in this study were originally obtained for a different study (Petterson et al. 2021) and re-used for the temporal sequence performance assessment. Both phantoms were installed in a mock-loop circulation (Mascarenhas et al. 2016). A pump was positioned proximal to the phantom that pumped water or physiological saline solution (9 g/L NaCl) through the printed AAA phantom or porcine aorta, respectively. On the distal end of the phantom, a three-element Windkessel model was placed to mimic the arterial compliance and peripheral resistance. A 3-D-printed spine was placed directly below both phantoms. The 3-D-printed AAA phantom was submerged in water, whereas the porcine aorta was placed in gelatin mixed with scatterers to imitate the surrounding soft tissues (Van Disseldorp et al. 2020a).

For both phantoms, a traditional 2-D+t acquisition was obtained, and one or three 3-D+t acquisitions were obtained for the porcine or the 3-D-printed phantom using different pulse wave rates, respectively. Between acquisitions, the pulse wave rate of the 3-D-printed AAA phantom was varied among 44, 54, 68 and 75 cycles/min, whereas for the AA porcine phantom the pulse wave rate was set to 75 cycles/min. In the 3-D-printed AAA phantom, for each appointed pulse wave rate, three separate acquisitions were obtained with different frame rates raging between 5 and 8 Hz. The frame rate was modified by changing the US acquisition depth and/or field-of-view opening angles. For the porcine phantom, only one 3-D+t acquisition was available, which was acquired with a frame rate of 4.5 Hz. The 2-D +t acquisitions were obtained with a frame rate of 62 or 30 Hz for the 3-D-printed AAA or AA porcine phantom, respectively. The 2-D+t acquisition was used as a ground truth for the sequenced 3-D+t acquisitions.

For the porcine phantom, estimation of 3-D radial strain was performed on the temporally sequenced data set to determine the potential of the increased frame rate when considering functional measurements. All sequenced frames were automatically segmented using the segmentation method described previously (Workflow Part 1: Temporal Sequencing). Subsequently, the frame-to-frame 3-D displacements were computed using a coarse-to-fine block matching approach (Lopata et al. 2009). The radial strains were calculated with respect to the phantom's wall contour centerline. For the temporally sequenced data set, the strain curve was computed by cumulatively summing the frame-to-frame strains. The end-systolic radial strain distributions obtained from the sequenced data sets were compared with a traditional strain estimation method, that is, radial strain estimation using 3-D displacements obtained directly from the end-diastolic to the end-systolic frame (Van Disseldorp et al. 2019).

Two groups of AAA patients were included retrospectively. The first group, included for temporal sequencing validation only, consisted of 25 AAA patients for whom the pulse wave rate was measured directly after the US exam. The second group was used for full workflow assessment and consisted of 37 different patients for whom two distinct acquisitions had been obtained of their AAA and a CT scan had been acquired within 3 months of the ultrasound acquisitions. The CT scans were obtained as part of normal clinical workflow, not specifically for this study. All US images were obtained during breath hold. The protocol was reviewed and approved by the local ethics committee of the Catharina Hospital Eindhoven. All patients gave informed consent, and the study was conducted according to the guidelines of the Declaration of Helsinki.

All ultrasound acquisitions were obtained using a matrix, phased array probe (X6-1, center frequency of 3.5×10^6 Hz) attached to an IU22 or EPIQ ultrasound system (Philips Ultrasound, Bothell, WA, USA). For the phantom experiments and first patient group, traditional acquisitions were obtained, that is, 3-D+t images from a single imaging position, whereas proximal and distal acquisitions were obtained for the second patient group. All acquisitions were obtained on a sagittal plane along the longitudinal axis of the AAA. In the trade-off between frame rate and spatial resolution, the image acquisition settings were chosen predominantly in favor of the frame rate. The frame rates of the acquisitions ranged between 3 and 8 Hz, and the total number of acquired 3-D frames within an acquisition ranged between 11 and 28. The voxel sizes were in the ranges of $0.3-0.6$ mm $\times$ $0.7-1.2$ mm $\times$ $0.6-1.3$ mm in the depth and length direction of the sagittal plane and width of the transverse plane, respectively, depending on the imaging depth and opening angle required to capture the AAA. The FOV opening angle in the transverse plane ranged between 53˚ and 90˚, whereas the sagittal plane the opening angle was always equal to 90˚. The

acquisitions were saved in DICOM format, exported to a PC and post-processed in MATLAB R2021a (The MathWorks, Natick, MA, USA).

The CT scans were obtained with a 256 iCT scanner (Philips Healthcare, Best, Netherlands), with a slice thickness of 3×10^{-3} m, a single collimation width of 0.625 mm, a total collimation width of 80 mm and voxel sizes of $0.73 \times 0.73 \times 3$ mm.

For the validation of the spatial registration workflow, the mean arterial pressure geometries of the fused proximal–distal AAA data sets were compared with CT scan-derived geometries, which is regarded as the golden standard for AAA geometry assessment, and with CT-matched ultrasound geometries obtained from traditional 3-D+t AAA images. All geometries were derived through segmentation of the inner aortic wall, as distinction between the outer wall and surrounding tissue is regularly challenging, as is the delineation between lumen and thrombus.

The fused and traditional AAA geometries were obtained using manual segmentation of frames obtained at mean arterial pressure, which was determined using the distension curves (Van Disseldorp et al. 2016b). During manual segmentation, first, the anterior and posterior AAA walls of two sagittal slices around the middle slice of the aneurysm volumes were delineated. These delineations were used as guidelines in the second step by depicting anterior and posterior points of the AAA in the transverse slices. Second, every fifth transverse slice in which the aneurysm was distinguishable was segmented manually by selecting points at distances of approximately 10 pixels. The obtained contours were upsampled in the Fourier domain and regularized by discarding all harmonics higher than 2. The time to complete a manual segmentation of a single AAA volume was approximately 20 min.

The CT scans were segmented semi-automatically using the software package Hemodyn (Philips Medical Systems) (Olabarriaga et al. 2004).

The US and CT segmentations were automatically aligned in three steps. First, the lateral translation was estimated by overlaying the maximum diameters of the AAA segmentations. Second, the endpoints of the wall contour centerlines of the geometries were registered to obtain the global rotation. Third, an iterative closest point algorithm was used for optimizing the US–CT geometry registration (Besl Paul and McKay 1992).

For the agreement analysis between the US- and CT-derived geometries, only the overlapping regions of the US and CT geometries were taken into account. For these overlapping regions, the similarity index (SI) and the 95th percentile Hausdorff distance (D_{95}) were computed using two equations:

$$\mathrm{SI} = \frac{2(N_{\mathrm{CT}} \cap N_{\mathrm{US}})}{N_{\mathrm{CT}} + N_{\mathrm{US}}} \tag{4}$$

where N_{CT} and N_{US} are the numbers of voxels in the CT and US geometry sections with overlapping longitudinal axis. The closer the SI value is to 1, the higher is the agreement between the two geometries; and

$$D_{95} = \left[{}^{95}K^{th}_{c \in C} d(c, U) \; + {}^{95}K^{th}_{u \in U} d(u, C)\right]/2 \tag{5}$$

where $d(c, U)$ is the distance from a point c within the CT geometry to the closest point U in the US geometry, and vice versa for $d(u, C)$. ${}^{95}K^{\mathrm{th}}$ represents the 95% ranked distance (Dubuisson and Jain 1994).

The possible presence of a monotonic relationship between the AAA's maximal diameter and/or tortuosity and the 95th percentile Hausdorff distance or similarity index was investigated using Spearman's correlation. The AAA's maximal diameter was obtained from the US images, and the tortuosity index was defined as the total AAA's CT-derived wall contour centerline length divided by the shortest distance between the outer ends of the centerline. In cases in which Spearman's correlation index is close to 1 or −1, there is a strong positive or negative monotonic relationship. In cases in which Spearman's correlation index is close to 0, no or a weak monotonic relationship is present.

RESULTS

The temporally sequenced 3-D-printed AAA and porcine AA phantom data are illustrated in Figure 4. On the left-hand side of the figure are the 2-D+t ultrasound images of the phantoms. In the middle are the 3-D+t distension curves for the different pulse wave rates and frame rates. The subfigures on the right illustrate the traditional 2-D+t distension curves and the temporally sequenced 3-D+t curves, which were obtained using different frame rates. The data points of the 3-D+t curves were given different colors to visualize the rearrangement of the distension curves (Fig. 4, middle) into the sequenced, single blood pulse wave cycle (Fig. 4, right).

The method proposed estimated the pulse wave rates for every 3-D+t phantom acquisition correctly. Accordingly, the temporal sequencing was performed correctly as seen in Figure 4. In the right subfigures, the sequenced 3-D+t curves closely resemble the traditional 2-D+t aortic distension curves. The colors of the 3-D+t data points in the subfigures in the middle column of the figure indicate that the points from specific parts of the blood pulse wave cycle were grouped together correctly in the temporally sequenced curve. Hence, temporal sequencing in the aortic phantoms had a success rate of a 100%.

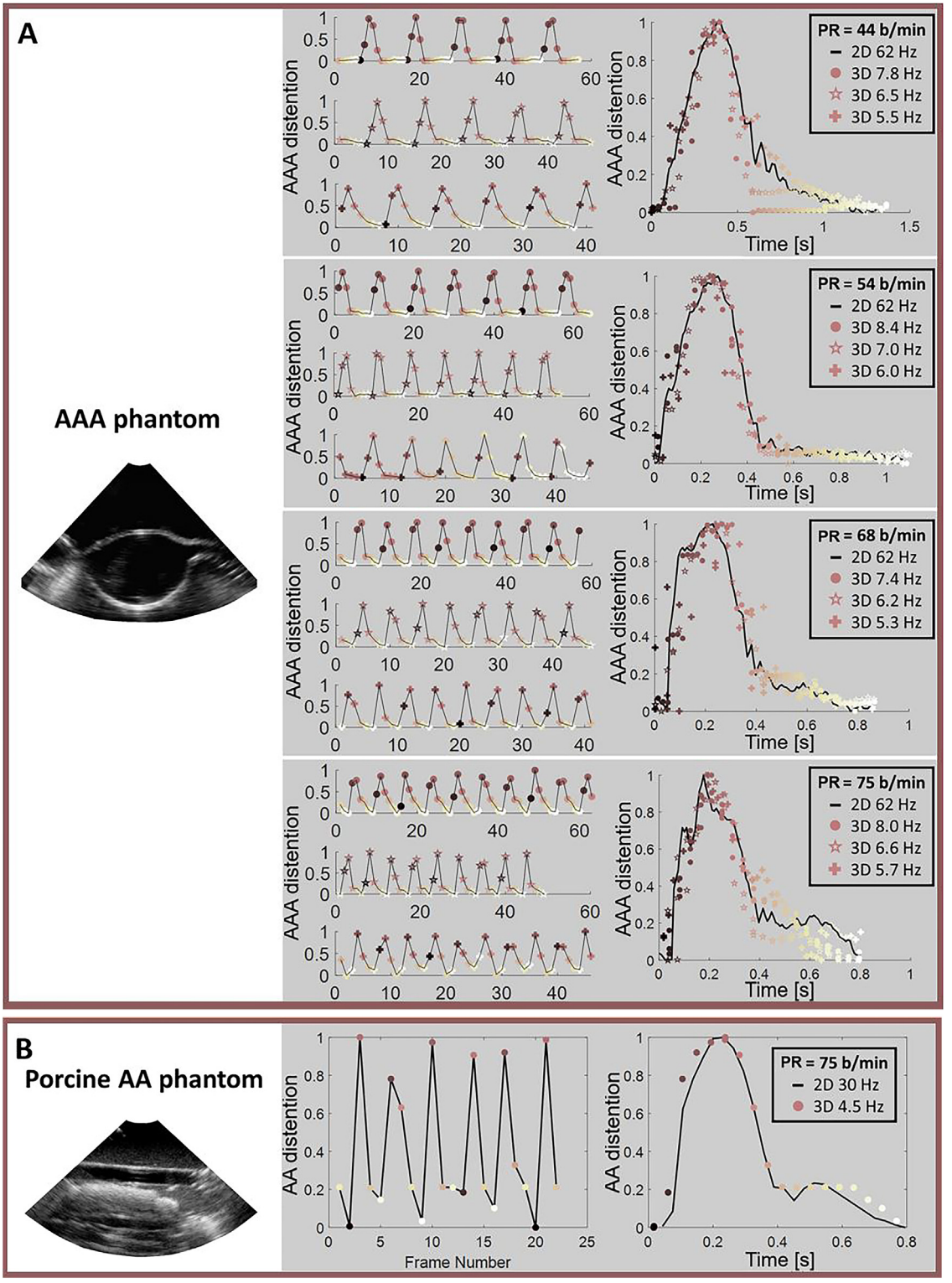

Fig. 4. Temporal sequencing results of the acquisitions of (A) the 3-D printed abdominal aortic aneurysm (AAA) phantom with varying pulse wave rates and frame rates and (B) the porcine AA phantom. Shown are the 2-D ultrasound images of the phantoms (left); 3-D+t aortic distension curves for the different phantoms, pulse wave rates and frame rates (middle); 2-D+t aortic distension curves (*black lines*) and the 3-D+t sequenced distension curves for the different frame rates (*red dots*) and pulse wave rates (*right*). The *red color spectrum* gives an indication of the rearrangement of the 3-D +t acquisitions into a single blood pulse wave cycle. PR = pulse rate.

The feasibility of radial strain estimation of the temporally sequenced data was determined using the porcine phantom ultrasound data. In contrast to the data for the AAA phantom and AAA patient, the porcine phantom's radial displacements were large enough for 3-D displacement tracking. Figure 5A illustrates the end-systolic strain distribution for the traditional method (*i.e.,* 3-D tracking directly from the end-diastolic to end-systolic frame), whereas Figure 5B illustrates the strain distribution for the 3-D+t sequenced data set. The strain distributions appear similar when considering the strain variation within the phantom's anterior and posterior walls. The average end-systolic strains obtained using the traditional method were 0.31 ± 0.03 and 0.16 ± 0.02 (mean± standard deviation) for the anterior and posterior walls, respectively. The average anterior and posterior end-systolic strains of the sequenced data set were 0.27 ± 0.07 and 0.12 ± 0.06 (mean ± standard deviation). Lateral displacement tracking failed because of the poor lateral wall contrast. Figure 5C illustrates the average anterior and posterior wall strain curves, which are impossible to obtain using the traditional method. The anterior wall strain is higher than the posterior wall strain.

Pulse wave rate estimation was also performed for the group of 25 patients for whom the pulse wave rate was measured directly after their US acquisition. For 20 of the 25 patients, the estimated pulse wave rate deviated within 0−5 cycles/min from the measured pulse wave rate. In five patients, the difference in estimated and measured pulse wave rates ranged between 9 and 25 cycles/min. For one patient, the pulse wave rate estimation failed, as the Lomb−Scargle periodogram was flat.

In the other patient group for which a proximal and a distal AAA acquisition were obtained, the

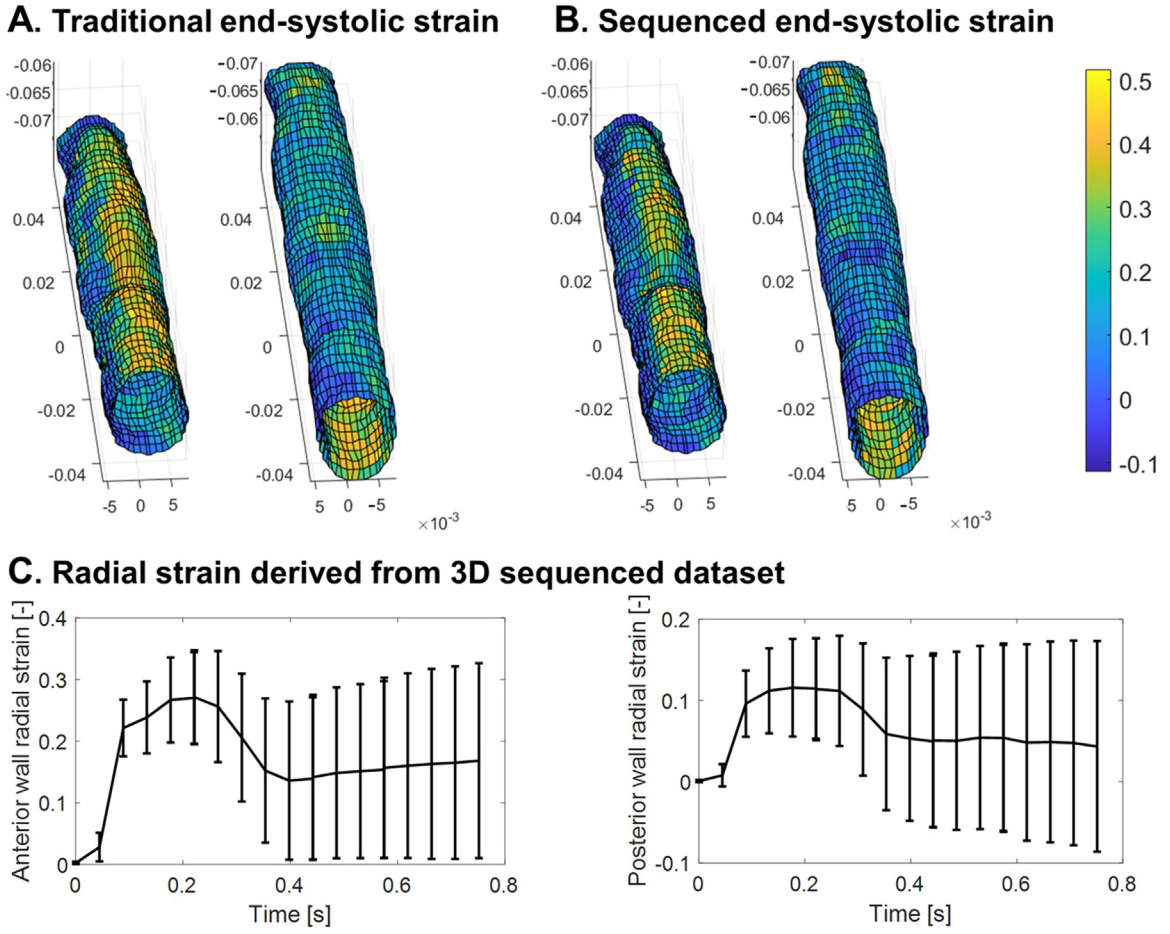

Fig. 5. Radial strain estimation derived from 3-D displacement tracking on the porcine phantom data set. (A) End-systolic radial strain distribution obtained using the traditional method (*i.e.,* 3-D displacement tracking directly from end-diastole to end-systole). The average end-systolic radial strains of the anterior (left subfigure) and posterior (right subfigure) walls are 0.31 ± 0.03 and 0.16 ± 0.02, respectively. (B) End-systolic radial strain distribution of the temporally sequenced data set, with average anterior (left subfigure) and posterior (right subfigure) strains of 0.27 ± 0.07 and 0.12 ± 0.06, respectively. (C) Anterior and posterior wall strain curves of the sequenced 3-D porcine phantom data set.

difference in pulse wave rates between the corresponding proximal and distal US acquisitions was 0−5 cycles/min in 31 patients and between 6 and 10 cycles/min in the other 6 patients. Furthermore, the frame rate of the sequenced acquisitions increased by a factor of 5, on average. After temporal registration, the frame rate was on average three times higher than the traditional frame rate (Fig. 6A). The mean pulse phase difference (*i.e.,* mean time interval) between consecutive frames, $\Sigma(p_i - p_{i-1})/n$) (where p is the pulse phase, i is the frame number and n is the number of frames), within the sequenced acquisition was on average 0.04, 0.04 and 0.05 for the proximal, distal and fused acquisitions, respectively, compared with 0.22 for the traditional acquisitions (Fig. 6B). The maximum pulse phase difference was on average 0.15, 0.11 and 0.15 for the proximal, distal and fused acquisitions, respectively, in comparison to 0.22 for the traditional acquisitions (Fig. 6C). In 4 patients, temporal registration resulted in a reduction in frame rate and large mean and maximal pulse phase differences, relative to the traditional acquisitions.

The mean and maximum pulse phase distances between corresponding proximal and distal time frames were on average 0.02 and 0.04, respectively.

The spatial registration algorithm was successful in 32 of 37 patients, 4 of whom required a slight manual adjustment. This adjustment consisted of manually choosing the best initial registration as the starting point for the translation fine-tuning, instead of using the trimmed-mean of all initial registration transforms. In two data sets, the unsuccessful registration was caused by very poor image quality in at least one of the acquisitions. In the other three unsuccessfully registered data sets, the few anatomical shapes present in the images were very similar, causing the algorithm to overlay them completely instead of placing them side-to-side in the proximal−distal direction.

For the registration method proposed, the 95th percentile Hausdorff distances and the similarity indices of the successfully registered data sets were 4.2 ± 1.7 mm and 0.92 ± 0.02 (median ± interquartile range), respectively (Fig. 7A, 7B), indicating high agreement between the corresponding US- and CT-derived geometries. Both parameters were in accordance with the CT-matched traditional ultrasound geometries, which displayed 95th percentile Hausdorff distances and similarity indices of 3.4 ± 1.2 mm and 0.93 ± 0.02, respectively. For five of the 32 traditional data sets, the US-to-CT volume

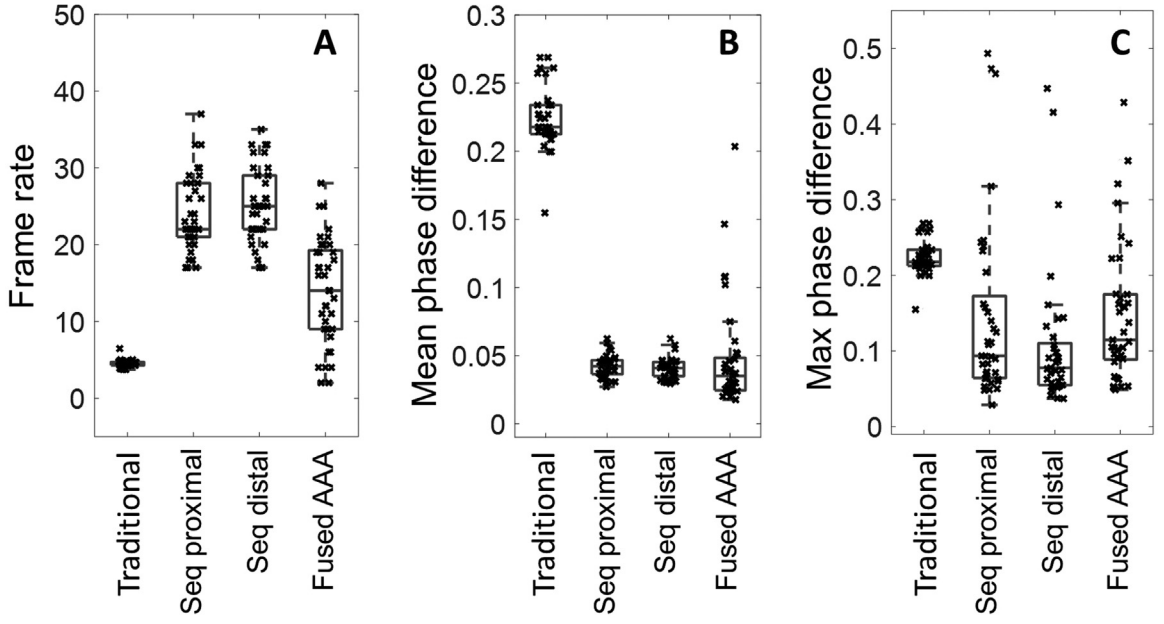

Fig. 6. Temporal sequencing and registration results of the second abdominal aortic aneurysm (AAA) patient group. (A) After temporal sequencing, the frame rate was increased by a factor of 5 on average with respect to that of the traditional data set. The frame rates of the temporally registered data sets were on average three times higher than that of the traditional data set. In four patients, the frame rate was reduced relative to those of the traditional data sets after temporal registration. (B) The mean pulse phase difference between frames within a data set was a factor of 4 lower for the sequenced data sets and all successfully temporally registered data sets. (C) The maximal pulse phase difference between consecutive frames in the sequenced and temporally registered data sets was on average twice as low as those of the traditional data sets.

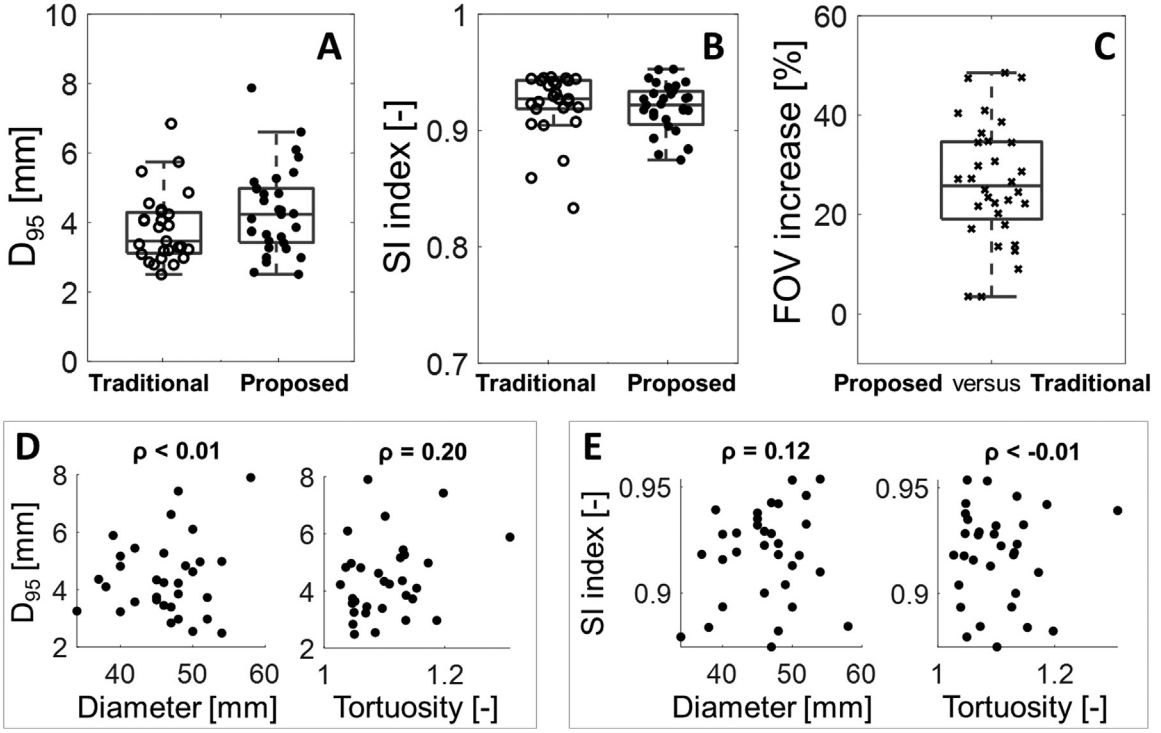

Fig. 7. Spatial registration results of the successfully registered data sets. (A) Ninety-fifth percentile Hausdorff distances of the traditional method and the method proposed. (B) Similarity indices (SI) of the traditional method and the method proposed between the corresponding computed tomography (CT)− and ultrasound (US)−derived geometries. (C) Field-of-view (FOV) increase after spatial registration. (D) Ninety-fifth percentile Hausdorff distance. (E) Plot of similarity index against AAA diameter and tortuosity index, with Spearman's ρ correlation.

registration failed because the US AAA volume was too small and its geometry too amorphous for accurate CT matching.

For the successfully registered proximal−distal images, the FOV increase ranged between 9% and 49% with respect to the traditional method (Fig. 7C). For two data sets, the FOV increase was only 3%. These two data sets are expected to just be a do-over, instead of the multi-perspective ultrasound acquisition required for a large AAA.

An investigation was conducted into whether there existed a monotonic relationship between the 95th percentile Hausdorff distance and AAA diameter and tortuosity (Fig. 7D) and similarity index and AAA diameter and tortuosity (Fig. 7E) using Spearman's correlation. Spearman's correlation indicated no monotonic relationship was present between any of the investigated parameter couples, with Spearman's correlation ρ being between −0.01 and 0.20. The unsuccessful registration data sets had diameters (tortuosity indices) of 33 mm (1.16), 38 mm (1.09), 46 mm (1.04), 48 mm (1.03) and 48 mm (1.20), which appear to be a random sample from the patient group.

DISCUSSION

Many studies have been contributing toward a patient-specific evaluation of AAA characteristics that can be performed using 3-D+t ultrasound. However, ultrasound is limited in its field of view and frame rate. The frame rate normally ranges between 3 and 8 Hz, hampering wall displacement estimation. Furthermore, in approximately 40%−45% of the AAAs, multiple acquisitions must be obtained to capture the full AAA geometry. Accordingly, in this study, a fully automatic algorithm was presented to increase the US frame rate and field of view using temporal sequencing and temporal and spatial registration.

The success of the temporal sequencing method is directly correlated to the accuracy of the pulse wave rate estimation. In both the 3-D-printed AAA and AA porcine phantoms, the pulse wave rate estimation was correct. It should be noted that although these phantoms simulate normal physiology, its relevance in the follow-up of AAA patients is confined, as the clinical interest is variation in AAA size and shape. In addition, pulse wave rate estimation was correct in 82% of all AAA patients. The lower success rate in AAA patients with respect to

the phantom measurements can be explained by the relatively lower image contrast and image quality. The poorer image quality was caused by the ultrasound signal traveling through fat and bowel tissue, whereas the surrounding medium in the phantoms consisted only of gelatin or water. Additionally, the pulse wave rate was constant in the phantoms, whereas in the patients slight pulse wave rate deviations occur. Accordingly, an instantaneous pulse wave rate estimation method could improve the temporal sequencing algorithm. However, for this application (*i.e.,* 3-D+t AAA imaging), the implementation of an instantaneous pulse wave rate estimation method is challenging because of the low frame rate, non−pulse-cycle-related AAA motion and accuracy of the AAA wall tracking.

The feasibility of radial strain estimation over time in 3-D volumes has been determined in a porcine abdominal aorta phantom. The 3-D end-systolic radial strain distribution was similar to the traditional method. Lateral tracking is hampered because of the poor lateral wall contrast, but might be improved in future studies by adding extra acquisitions obtained serially in the transverse plane from different insonification angles. The anterior wall strains were higher than the posterior wall strains, which was as expected based on previous studies (Petterson et al. 2021). The average strain values did not return to zero, which is likely caused by accumulation of displacement errors over time. Unfortunately, strain estimation of the temporally sequenced AAA phantom and patient data sets was because of the limited spatial resolution of the 3-D DICOM images. The feasibility of 3-D strain estimation of temporally sequenced AAA patient data sets should be investigated in future research using raw frequency data.

The pulse phase estimation has also been found to be correct when comparing frame positions within their original 3-D AAA distension curve with its new position in the sequenced distension curve. After sequencing, the frame rate was increased fivefold, the mean pulse phase difference (*i.e.,* mean time interval) between frames within a data set was reduce by a factor of 4 and the maximal phase difference between frames was on average twice as low with respect to that of the traditional method. However, after temporal registration, the frame rate of the fused AAA acquisitions was only three times as high. This difference in frame rate increase is caused by the clustering of frames in pulse wave phase. In other words, for specific combinations of frame rate and pulse wave rate, the sequenced frames will be overlain or packed closely together in the blood pulse wave cycle in a few distinct clusters with a large maximal pulse phase between the clusters (*e.g.,* a frame rate of 8 Hz in combination with a heart rate of 80 beats/min results in only six distinct, evenly spread pulse phases). In these cases, the frame rate after temporal registration exhibited a limited increase or even a decline. In four patients, all frames were clustered into two or three groups within the blood pulse wave cycle, causing a reduction in the frame rate of the fused AAA data set with respect to the traditional data set. This clustering of frames in the blood pulse wave cycle can be prevented by, first, estimating the patient's heart rate using, for example, a blood pressure monitor, smart watch or electrocardiogram. Subsequently, the desired AAA ultrasound field of view should be determined and the corresponding frame rate (f_{s1}) for this specific FOV should be read from the ultrasound machine's screen. Then, the frame rate range ($f_{s2}-f_{s1}$) in which the optimal frame rate is situated can be determined using

$$f_{s2} = f_{HR} \cdot (f_{s1}/f_{HR} - 1) \tag{6}$$

where f_{HR} is the heart rate (in Hz), f_{s1} the initial frame rate (in Hz) depicted on the ultrasound machine and f_{s2} the estimated lower limit of the frame rate range (in Hz). Finally, the optimal frame rate leading to the best possible spread in, and number of, distinct pulse phase frames obtained with minimal clinical and computational effort is the integer in the range $f_{s2}-f_{s1}$, which can be obtained by increasing the field of view slightly. Although the acquisition frame rate is most likely not an integer, even though the ultrasound machine's screen depicts it as one, the estimated frame rate using this method is still expected to prevent frame clustering in most situations.

Spatial registration was successful in 32 of the 37 patients. The judgment of the registration performance was based on visual inspection of the registered images and whether it was possible to segment them. The five unsuccessful segmentations were caused by the duplication of visible anatomical structures resulting from incorrect spatial registration. Accordingly, for these data sets, computing the 95th percentile Hausdorff distance and the similarity index was impossible.

For the successful registered data sets, the 95th percentile Hausdorff distances were small, and there was one outlier caused by poor lateral image contrast. In addition, the similarity indices were close to its maximum of 1. Hence, the US- and corresponding CT-derived segmentations were in good agreement, supporting the claim of correct multi-perspective spatial registration. Furthermore, the multi-perspective 95th percentile Hausdorff distances and similarity indices were in accordance with the indices obtained from the CT-matched traditional ultrasound-derived geometries and not correlated to the AAA's diameter or tortuosity.

Registration error estimation of the specific AAA regions (*e.g.,* lateral wall, proximal or distal region) would be interesting. Unfortunately, this estimation is cumbersome in patients because of the unclear origin of

the error, for example, proximal−distal US registration, US−CT registration and/or US-/CT-segmentation, in combination with the relatively poor image quality and lateral wall contrast.

In the data sets in which similarly shaped structures were wrongly registered, another relatively high peak within the (cylindrical) phase correlation spectrum might provide the correct rotation and/or translation.

The execution time for the entire workflow when run on a Dell computer with an Intel Core i7 2.80-GHz processor and 16 GB RAM is approximately 2 h per data set, of which 15 min is used for pre-processing, 45 min for temporal and spatial registration and 1 h for fusion of all volumes. Currently, the algorithm is designed for accuracy without considering computational efficiency very thoroughly. Therefore, the execution time can be reduced by optimizing the algorithm, by using parallel processing on a GPU and/or making the algorithm more computationally efficient.

In future studies, the lateral contrast of the US volumes and, thus, US geometry derivation could be enhanced using additional ultrasound acquisitions with different insonification angles. In addition, for the proximal−distal acquisitions, the probe could be slightly tilted outward to capture the aneurysm's edges with higher contrast, though this might lead to a reduction in spatial registration performance of the workflow proposed because of a lower similarity between visible anatomical structures.

The success rate of the spatial registration might be improved using a single 3-D volume acquisition with a larger coverage in transverse and sagittal planes per proximal and distal probe position, in addition to the 3-D +t proximal and distal acquisitions. These 3-D acquisitions should be acquired from the same probe positions as the 3-D+t data sets and could be used during the initial spatial registration, after which immediately the translational fine-tuning of the paired 3-D+t proximal and distal frame sets can be executed.

Deep learning models could also improve the robustness and performance of the algorithm in terms of pulse wave rate estimation and spatial registration. However, a ground truth training data set should be obtained, which could be challenging.

Furthermore, AAA patient-specific material property estimation could be improved using the method proposed in this study, which should be assessed in future studies.

CONCLUSIONS

The workflow proposed successfully performed spatial and temporal registration of AAA multi-perspective 3-D+t US acquisitions, in which both the field of view and temporal resolution were increased. The field of view can be enlarged to capture a larger part or the entire aneurysm, and the temporal resolution was increased by a factor of 3. Temporal sequencing could also be applied to individual acquisitions, increasing their frame rates by a factor of 5, on average. The workflow proposed enables AAA patient-specific material property analysis and growth evaluation for patients with all AAA sizes, using cheap and non-invasive 3-D+t US acquisitions.

Acknowledgments—This work is part of the Multiperspective Ultrasound Strain Imaging & Elastography (MUSE) project, which has received funding from the European Research Council (ERC) under the European Union's Horizon 2020 Research and Innovation Programme (ERC Starting Grant 757958).

Conflict of interest disclosure—The authors declare they have no conflicts of interest.

REFERENCES

Alvarez L, Guichard F, Lions PL, Morel JM. Axioms and fundamental equations of image processing. Arch Ration Mech Anal 1993;123:199–257.

Anders W, Fabio V, Van Herzeele I, Allaire E, Bown M, Cohnert T, Dick F, van Herwaarden J, Karkos C, Koelemay M Kölbel T, Loftus I, Mani K, Melissano G, Powell J, Szeberin Z. European Society for Vascular Surgery (ESVS) 2019 Clinical Practice Guidelines on the Management of Abdominal Aorto-iliac Artery Aneurysms. Eur J Vasc Endovasc Surg 2018;57:1–97.

Baba K, Kobayashi K, Hayashi M, Kozuma S, Takeda S, Kinoshita K. Extended field-of-view ultrasound imaging in obstetrics and gynecology: Preliminary experience. Ultrasound Obstet Gynecol 2000;15:157–159.

Barberie JE, Wong A, Cooperberg P, Carson B. Extended field-of-view sonography in musculoskeletal disorders. AJR Am J Roentgenol 1998;171:751–757.

Besl Paul J, McKay ND. A method for registration of 3-D shapes. IEEE Trans Pattern Anal Mach Intell 1992;14:239–256.

Chaikof EL, Dalman RL, Eskandari MK, Jackson BM, Lee WA, Mansour MA, Mastracci TM, Mell M, Murad MH, Nguyen LL, Oderich GS, Patel MS, Schermerhorn ML, Starnes BW. The Society for Vascular Surgery Practice Guidelines on the Care of Patients with an Abdominal Aortic Aneurysm. J Vasc Surg 2018;67:2–77.

De Hoop H, Petterson NJ, Van De Vosse FN, Van Sambeek MR, Schwab HM, Lopata RG. Multiperspective ultrasound strain imaging of the abdominal aorta. IEEE Trans Med Imaging 2020;39:3714–3724.

De Ruijter J, van Sambeek M, van de Vosse F, Lopata R. Automated 3D geometry segmentation of the healthy and diseased carotid artery in free hand, probe tracked ultrasound images. Med Phys 2020;47:1034–1047.

Dubuisson MP, Jain AK. A modified Hausdorff distance for object matching. In: Proceedings, 12th International Conference on Pattern Recognition. New York. : IEEE; 1994. p. 566–568. volume 1.

Elliott S. A user guide to extended field of view in ultrasonography. Ultrasound 2006;14:55–58.

Erhart P, Hyhlik-Dürr A, Geisbüsch P, Kotelis D, Müller-Eschner M, Gasser TC, von Tengg-Kobligk H, Böckler D. Finite element analysis in asymptomatic, symptomatic, and ruptured abdominal aortic aneurysms: in search of new rupture risk predictors. Eur J Vasc Endovasc Surg 2015;49:239–245.

Fillinger MF, Marra SP, Raghavan ML, Kennedy FE. Prediction of rupture risk in abdominal aortic aneurysm during observation: Wall stress versus diameter. J Vasc Surg 2003;37:724–732.

Gasser TC. Biomechanical rupture risk assessment: A consistent and objective decision-making tool for abdominal aortic aneurysm patients. AORTA J 2016;4:42.
Han HC, Fung YC. Longitudinal strain of canine and porcine aortas. J Biomech 1995;28:637–641.
Indrakusuma R, Jalalzadeh H, Planken R, Marquering H, Legemate D, Koelemay M, Balm R. Biomechanical imaging markers as predictors of abdominal aortic aneurysm growth or rupture: A systematic review. Eur J Vasc Endovasc Surg 2016;52:475–486.
Karatolios K, Wittek A, Nwe TH, Bihari P, Shelke A, Josef D, Schmitz-Rixen T, Geks J, Maisch B, Blase C, Moosdorf R, Vogt S. Method for aortic wall strain measurement with three-dimensional ultrasound speckle tracking and fitted finite element analysis. Ann Thorac Surg 2013;96:1664–1671.
Kauffmann C, Tang A, Therasse E, Giroux MF, Elkouri S, Melanson P, Melanson B, Oliva VL, Soulez G. Measurements and detection of abdominal aortic aneurysm growth: Accuracy and reproducibility of a segmentation software. Eur J Radiol 2012;81:1688–1694.
Lederle FA, Wilson SE, Johnson GR, Reinke DB, Littooy FN, Acher CW, Ballard DJ, Messina LM, Gordon IL, Chute EP, Krupski WC, Busuttil SJ, Barone GW, Sparks S, Graham LM, Rapp JH, Makaroun MS, Moneta GL, Cambria RA, Makhoul RG, Eton D, Ansel HJ, Freischlag JA. Bandyk D, for the Aneurysm Detection and Management Affairs Cooperative Study Group. Immediate repair compared with surveillance of small abdominal aortic aneurysms. N Engl J Med 2002;346:1437–1444.
Lomb NR. Least-squares frequency analysis of unequally spaced data. Astrophys Space Sci 1976;39:447–462.
Lopata RG, Nillesen MM, Hansen HH, Gerrits IH, Thijssen JM, De Korte CL. Performance evaluation of methods for two-dimensional displacement and strain estimation using ultrasound radio frequency data. Ultrasound Med Biol 2009;35:796–812.
Mascarenhas EJ, Peters MF, Nijs J, Rutten MC, van de Vosse FN, Lopata RG. Assessment of mechanical properties of porcine aortas under physiological loading conditions using vascular elastography. J Mech Behav Biomed Mater 2016;59:185–196.
Merkx M, van't Veer M, Speelman L, Breeuwer M, Buth J, Van De Vosse F. Importance of initial stress for abdominal aortic aneurysm wall motion: Dynamic MRI validated finite element analysis. J Biomech 2009;42:2369–2373.
Niklaus S, Mai L, Liu F. Video frame interpolation via adaptive separable convolution. In: Proceedings of the IEEE International Conference on Computer Vision. New York. : IEEE; 2017. p. 261–270.
Olabarriaga SD, Breeuwer M, Niessen WJ. Segmentation of abdominal aortic aneurysms with a non-parametric appearance model. Computer Vision and Mathematical Methods in Medical and Biomedical Image Analysis. Berlin/Heidelberg: Springer; 2004. p. 257–268.
Petterson N, Sjoerdsma M, van Sambeek M, van de Vosse F, Lopata R. Mechanical characterization of abdominal aortas using multiperspective ultrasound imaging. J Mech Behav Biomed Mater 2021;119 104509.
Raghavan M, Vorp DA. Toward a biomechanical tool to evaluate rupture potential of abdominal aortic aneurysm: Identification of a finite strain constitutive model and evaluation of its applicability. J Biomech 2000;33:475–482.
Rana M, Wakeling JM. In-vivo determination of 3D muscle architecture of human muscle using free hand ultrasound. J Biomech 2011;44:2129–2135.
Reed WW, Hallett JW, Damiano MA, Ballard DJ. Learning from the last ultrasound: A population-based study of patients with abdominal aortic aneurysm. Arch Intern Med 1997;157:2064–2068.
Reimerink JJ, van der Laan MJ, Koelemay MJ, Balm R, Legemate DA. Systematic review and meta-analysis of population-based mortality from ruptured abdominal aortic aneurysm. J Br Surg 2013;100:1405–1413.
Senouf O, Vedula S, Zurakhov G, Bronstein A, ZibulevskyM Michailovich O, Adam D, Blondheim D. High frame-rate cardiac ultrasound imaging with deep learning. International Conference on Medical Image Computing and Computer-Assisted Intervention. Berlin/Heidelberg: Springer; 2018. p. 126–134.
Simoncelli EP, Freeman WT. The steerable pyramid: A flexible architecture for multi-scale derivative computation. In: Proceedings, International Conference on Image Processing. New York: IEEE; 1995. p. 444–447. volume 3.
Van den Heuvel TL, Petros H, Santini S, de Korte CL, van Ginneken B. Automated fetal head detection and circumference estimation from free hand ultrasound sweeps using deep learning in resource-limited countries. Ultrasound Med Biol 2019;45:773–785.
Van Disseldorp EM, Hobelman KH, Petterson NJ, van de Vosse FN, van Sambeek MR, Lopata RG. Influence of limited field-of-view on wall stress analysis in abdominal aortic aneurysms. J Biomech 2016;49:2405–2412.
Van Disseldorp E, Petterson N, Rutten M, Van De Vosse F, van Sambeek M, Lopata R. Patient specific wall stress analysis and mechanical characterization of abdominal aortic aneurysms using 4D ultrasound. Eur J Vasc Endovasc Surg 2016;52:635–642.
Van Disseldorp EM, Petterson NJ, van de Vosse FN, van Sambeek MR, Lopata RG. Quantification of aortic stiffness and wall stress in healthy volunteers and abdominal aortic aneurysm patients using time-resolved 3D ultrasound: A comparison study. Eur Heart J Cardiovasc Imaging 2019;20:185–191.
Van Disseldorp EM, van den Hoven MH, van de Vosse FN, van Sambeek MR, Lopata RG. Reproducibility assessment of ultrasound-based aortic stiffness quantification and verification using bi-axial tensile testing. J Mech Behav Biomed Mater 2020;103 103571.
Van Disseldorp EM, van Dronkelaar JJ, Pluim JP, van de Vosse FN, van Sambeek MR, Lopata RG. Ultrasound based wall stress analysis of abdominal aortic aneurysms using multiperspective imaging. Eur J Vasc Endovasc Surg 2020;59:81–91.
Wilson KA, Lee AJ, Hoskins PR, Fowkes FGR, Ruckley CV, Bradbury AW. The relationship between aortic wall distensibility and rupture of infrarenal abdominal aortic aneurysm. J Vasc Surg 2003;37:112–117.
Wittek A, Karatolios K, Bihari P, Schmitz-Rixen T, Moosdorf R, Vogt S, Blase C. In vivo determination of elastic properties of the human aorta based on 4D ultrasound data. J Mech Behav Biomed Mater 2013;27:167–183.
Xiao G, Brady JM, Noble JA, Burcher M, English R. Nonrigid registration of 3-D free-hand ultrasound images of the breast. IEEE Trans Med Imaging 2002;21:405–412.
Yang M, Sampson R, Wei S, Wenisch TF, Fowlkes B, Kripfgans O, Chakrabarti C. High volume rate, high resolution 3D plane wave imaging. Proc IEEE Int Ultrason Symp 2014;1253–1256.
Yerli H, Eksioglu SY. Extended field-of-view sonography: Evaluation of the superficial lesions. Can Assoc Radiol J 2009;60:35–39.
Zhang X, Homma N, Abe M, Sugita N, Takai Y, Narita Y, Yoshizawa M. Volume registration based on 3-D phase correlation for tumor motion estimation in 4-D CT. 2013 35th Annual International Conference of the IEEE Engineering in Medicine and Biology Society (EMBC). New York. : IEEE; 2013. p. 5095–5098.
Zielinski AH, Ghulam Q, Bredahl KK, Rouet L, Dufour C, Sillesen HH, Eiberg JP. Improved volume assessment of abdominal aortic aneurysms using a new acquisition protocol combining three-dimensional ultrasound and magnetic field tracking—The first results of a clinical feasibility study. Eur J Vasc Endovasc Surg 2019;58:e612–e613.